Soft Matter

ARTICLE TYPE

Cite this: DOI: 10.1039/xxxxxxxxxx

Stretching and breaking of PEO nanofibres. A classical force field and ab-initio simulation study

Eivind Bering,*[a] and Astrid S. de Wijn[b]

Received Date
Accepted Date

DOI: 10.1039/xxxxxxxxxx

www.rsc.org/journalname

The burgeoning development of nanotechnology is allowing us to construct more and more nanoscale systems in the real world that used to only exist in computer simulations. Among them, nanofibres made of only a few aligned polymeric chains in particular might soon cover important roles in nanofabrications as well as in nanomedicine. In this work, we present a broad exploration by computer simulations of elastic and inelastic properties of polyethylene-oxide (PEO) nanofibres under load. We cover the full range from unloaded fibres up to their breaking point, focusing on all features that arise from chain-chain interactions and collective behaviour of the chains. We employ both molecular dynamics (MD) simulations and density functional theory (DF). The classical force field is represented by a minimal reactive force field model, allowing for the breaking of covalent bonds. Density functional (DF) computations provide a benchmark to gauge and validate the empirical force field approach, and offer an intriguing view of the bundle chemical evolution after breaking. Force-field based MD is employed for the systematic investigation of bundles of up to 24 chains, and for a single bundle of 100 chains. Low-temperature results for bundles under moderate loading provide a size-dependent sequence of cross-sections, structures, cohesive energies and elastic properties. A remarkably high Youngs modulus on the order of 100 GPa was estimated with DF and MD, explained by the semi-crystalline state of the fibres giving mechanical properties comparable to those of carbon nanotubes and of graphene. Breaking is investigated by simulations with constant strain rate or constant stress. The bundle breaks whenever the potential energy is raised above its metastability range, but also below that limit due to creep activated by thermal fluctuations. A Kramers-type approximation for the rate of chain breaking is proposed and compared to simulation data.

1 Introduction

Polymers underlie a vast variety of industrial applications[1]. They also represent an essential ingredient of life, since proteins, nucleic acids and polysaccharides consist of polymeric molecules.[2] The mechanical properties of polymers play an important role in their function, in both the man-made and natural context.[3] Experimental developments in nanotechnology and biophysics as well as the overwhelming growth of computer power are making it feasible to investigate the mechanical properties of polymer fibres down to the molecular and atomistic scale.

Experimental measurements at the nano scale have been focused very heavily on the single molecule limit, using vibrational spectroscopy, atomic force microscopy and optical tweezers to determine the strain-stress relation in organic polymers and in biopolymers.[4,5] Measurements provide elastic properties and limiting resistance that can be compared with state of the art ab-initio computations,[6] but also highlight the difference with the same properties measured for macroscopic samples of the same material. In between the single molecule and the bulk are different structures and length scales that play a big role in this difference. This range of multiple chains together evokes the image of rope or yarn, which is often plied, consisting of macroscopic fibres twisted together to increase the strength and integrity of the final material. Similarly, the interaction and collective behaviour of the molecules inside polymer bundles play a crucial role in the mechanical properties of the nanometric bundle.

While these intermediate length scales have not been studied nearly as much as the single-molecule case, they are becoming experimentally accessible as well. Advanced fabrication techniques such as electrospinning allow the routine preparation of fibres of sub-μm length and diameter, reaching down to the 10 nm range.[7] This size still corresponds to hundreds of polymer chains, leaving out a relatively wide range that is currently accessible only to self-assembly, that, however, is available only for selected, mainly biological, polymers.

[a] NTNU, Department of Physics, PoreLab, S.P. Andersens vei 15 B, 7031 Trondheim, Norway. E-mail: eivind.bering@ntnu.no
[b] NTNU, Department of Mechanical and Industrial Engineering, Richard Birkelands vei 2B, 7034 Trondheim, Norway. E-mail: astrid.dewijn@ntnu.no

From a theoretical point of view, bundles in this size range are complex and therefore challenging. Important roles are played by chain-chain interactions, surface effects, entropy, nonlinearities, and thermal fluctuations. At the same time, the systems are so large as to be computationally expensive, yet too far from the thermodynamic limit to allow for standard approaches from statistical physics and thermodynamics. This regime of nano-scale bundles of small numbers of molecules (as opposed to single molecules[8] or bulk[9,10]) has not been investigated much theoretically.

In our computational study, we consider nanofibres of a simple paradigmatic polymer, i.e., polyethylene oxide (PEO), made of nanometric bundles, stretched between two rigid, planar clamps. PEO (also referred to as polyelthelene glycol or PEG) has a wide range of applications[11], and typing "polyethylene glycol" in an internet search engine in October 2019 produces about six million hits. It has been studied extensively experimentally[5,12]. In our simulations, we focus on the elastic and inelastic response of these nanofibres to tensile load, covering the creep regime and up to their limiting resistance and chemistry of breaking.

Basic bonding and elastic properties of very thin samples are analysed by density-functional (DF) simulations. This approach provides quantitative and predictive information on the interplay of different deformation modes such as torsion, bending and stretching along the chain, on the role of electron orbitals and covalent bonds in determining the chain breaking mechanism, deformation under stretching, and the re-bonding of chains after breaking.

We study somewhat larger bundles using a reactive classical force field, stretching them until they break. The stretched bundles exhibit a complex structure in the lateral direction, showing solid-like structures. In addition, we show that there are more complex structural effects in 3D, related to the helicity of the chains. The mechanical properties depend nontrivially on the number of chains in the bundle. Finally, we also investigate the thermal effects on the structure and breaking of bundles. We show, among other things, that imperfections in the structure impact on the mechanical properties.

The combination of chemical detail and accuracy provided by DF with the computational efficiency, and rigorous statistical mechanics framework provided by MD simulation offers a comprehensive view of a complex phenomenon such as creep in polymers.[13,14]

2 Method

We perform molecular dynamics (MD) simulations of stretching of a nanofibre of poly-ethylene oxide (PEO) composed of N molecular chains on the form $CH_3-[O-CH_2-CH_2]_n-O-CH_3$ with $n = 33$.

In our study, a tensile load or strain is applied to the PEO fibre through planar clamps. These clamps consist of a geometrical constraint on one of the coordinates, here z, of the terminations. The position of the carbon atoms belonging to the two terminal methyl groups are constrained to lay in the plane defining the clamps. The junction of chain and clamp can move along the plane of the clamp, hence tension combines with inter-chain cohesion to mimic lateral compression of the fibre. The simulations are carried out using the free and open-source LAMMPS Molecular Dynamics Simulator.[15] A sketch of this model is shown in Fig. 1.

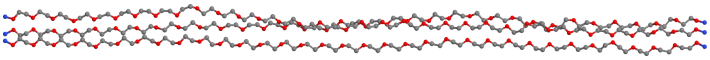

Fig. 1 A snapshot of a bundle with three chains.

2.1 Classical simulations

The polymeric PEO chains are described with a united atom model where each carbon is grouped with its bonded hydrogen atoms to form a united atom. It has been shown that this united-atom representation provides results in reasonable agreement with available experimental data at lower computational cost.[16] The basic force field we use has a functional form that resembles the OPLS model,[17] with some important distinctions. The potential energy surface is dividend into bonded and non-bonded parts,

$$U(\{\mathbf{R_i}, i=1,N\}) = U_{\text{bond}}(\{\mathbf{R_i}, i=1,N\}) + U_{\text{non-bond}}(\{\mathbf{R_i}, i=1,N\}) \,, \tag{1}$$

where $\mathbf{R_i}$ is the position of the i-th atom. The non-bonded part accounts for Coulomb interaction, short range repulsion, and dispersion interactions. The latter two are described by a Lennard-Jones pair potential, so that

$$U_{\text{non-bond}}(\{\mathbf{R_i}, i=1,N\}) = U_C(\{\mathbf{R_i}\}) + U_{LJ}(\{\mathbf{R_i}\}) \,, \tag{2}$$

where

$$U_{\text{C}}(\{\mathbf{R_i}\}) = k_{\text{e}} {\sum_{i\neq j}}' \frac{q_i q_j}{|\mathbf{R_i} - \mathbf{R_j}|} \tag{3}$$

and

$$U_{\text{LJ}}(\{\mathbf{R_i}\}) = 4 {\sum_{i\neq j}}' \varepsilon_{ij} \left[\left(\frac{\sigma_{ij}}{|\mathbf{R_i} - \mathbf{R_j}|} \right)^{12} - \left(\frac{\sigma_{ij}}{|\mathbf{R_i} - \mathbf{R_j}|} \right)^{6} \right] \,, \tag{4}$$

where k_{e} is the Coulomb constant, $\{q_i\}$ are atomic charges, σ_{ij} and ε_{ij} are the length and energy scales of the LJ potential. The prime on each sum indicates that pairs of atoms separated by one, two, or three consecutive bonds are excluded. This is the typical CHARMM convention.[18] The interaction energy between two dissimilar non-bonded atoms is estimated by the Lorentz-Berthelot combination rules, i.e. $\sigma_{ij} = \frac{\sigma_{ii}+\sigma_{jj}}{2}$ and $\varepsilon_{ij} = \sqrt{\varepsilon_{ii}\varepsilon_{jj}}$.[19]

The bonded interaction consist of stretching, bending and torsional contributions

$$U_{\text{bond}}(\{\mathbf{R_i}, i=1,N\}) = U_{\text{str}}(\{\mathbf{R_i}\}) + U_{\text{bend}}(\{\mathbf{R_i}\}) + U_{\text{tors}}(\{\mathbf{R_i}\}. \tag{5}$$

where each term is given by a quadratic function of the deviation of bond lengths and distances from their equilibrium value.

While a conventional quadratic bond stretching potential provides a fair description of the low energy portion of the system potential energy surface, it does not account for the anharmonicity of real bonds under high stress, and in particular it does not allow for bond breaking, which is what we are concerned with in

this work. In our minimal reactive force field, we therefore replace the conventional quadratic form of standard bond stretching potential with a Morse potential

$$U_{\rm str}(\{\mathbf{R_i}, i=1,N\}) = D_{ij}\left[1-e^{-\alpha_{ij}(r_{ij}-\bar{r}_{ij})}\right]^2 , \qquad (6)$$

which saturates to a finite value at large separations. Here D_{ij} is the dissociation energy, $\bar{r}_{ij}$ is the equilibrium bond distance and α_{ij} gives the width of the potential. If the bond length reaches a certain cut-off distance the bond is permanently removed. For these simulations a cut-off distance of 4 Å was used. For the C-C bond, this effectively reduces the dissociation energy by 2%. As is conventional, we do not take into account the zero point energy of the vibrational levels of around 4 kJ/mol. The required parameters for the dissociation energy D_{ij} are obtained from density functional computations of the same bond breaking,[20] and the parameters for α_{ij} are found by requiring the Morse potential to have the same curvature in the minimum as the harmonic bond, i.e. $\alpha_{ij} = \sqrt{K^{\rm s}_{ij}/2D_{ij}}$, where $K^{\rm s}_{ij}$ is the force constant in the harmonic potential

$$U_{\rm harmonic}(\{\mathbf{R_i}\}) = \frac{1}{2}\sum_{\{ij\}} K^{\rm s}_{ij}[r_{ij}-\bar{r}_{ij}]^2. \qquad (7)$$

The stress on end-bonds joining chains to the clamps is enhanced by inertia effects. To avoid their preferential breaking, these bonds are modeled with the harmonic potential. Our model covers only the C-C and C-O bond breaking events ofăinterest for our study. Bond-order force fields such as ReaxFF[21] could provide a more comprehensive view. However, this simple reactive force-field suffices for our purposes.

The potentials for the bending and torsion read

$$U_{\rm bend}(\{\mathbf{R_i}\}) = \frac{1}{2}\sum_{\{ijk\}} K^{\rm b}_{ijk}[\theta_{ijk}-\bar{\theta}_{ijk}]^2 \qquad (8)$$

and

$$U_{\rm tors}(\{\mathbf{R_i}\}) = \sum_{\{ijkl\}}\sum_{\{c\}} K^{{\rm t},c}_{ijkl}[\cos(\phi_{ijkl})]^{c-1} , \qquad (9)$$

where i, j, k and l are atoms joined by consecutive covalent bonds, $K^{\rm b}_{ijk}$ and $K^{\rm t}_{ijkl}$ are force constants of bending and torsion energy contributions and $\bar{\theta}_{ijk}$ are equilibrium angles. These are chosen to reproduce molecular properties measured by spectroscopy or computed by *ab-initio* methods. Note that the sum over the torsional coefficients includes every possible dihedral.ăMoreover, bending and torsion terms are not removed whenever a bond breaks.ăThis introduces a slight artifact into the potential energy surface, whose eliminationăwould require recoding the computation of the angular part of energy and forces.

This united atom force field parameterization is taken from van Zon *et al.*,[22] based on a modification of the explicit atom force field of Neyertz et al.[23] The set of parameters used in our simulations is reported in Table 1 and 2. The time step used in the simulations is 1 fs.

The initial configuration of the bundles is generated by placing the end particles randomly within circular cross sections of area of 16 Å^2 per chain, and the rest of the beads in chain are placed at equidistant spacing in the z-direction with a random component in the xy-plane.

Table 1 Force field parameters for the stretching, bending and for the non-bonded interaction[16] with disassociation energies[20]

Bonds	K^s_{ij} [kJ/(mol Å^2)]	D_{ij} [kJ/mol]	$\bar{r}_{ij}$ [Å]
C–C	2587.4	370.8	1.54
C–O	3094.0	344.5	1.43

Bends	K^b_{ijk} [kJ/mol]	$\bar{\theta}_{ijk}$ [Å]
O–C–C	727.7	110.0
C–O–C	1070.1	112.0

LJ-interaction	σ_{ii} [Å]	ε_{ii} [kJ/mol]	q_i [q_e]
CH_3	3.699	1.047	0.174
CH_2	3.624	0.831	0.174
O	3.034	0.401	-0.348

From the beginning of the simulation the fibers are stretched between the two clamps. This is somewhat artificial, since polymer chains at low strain tend to adopt a (nearly)-Gaussian coil configuration, however it might correspond well to stretching experiments using tweezers or AFM.

From these initial configurations the systems are subjected to simulated annealing to reach low-energy structures closer to equilibrium and what one would expect for experimental samples.[24] During this process the Morse potential for the bond stretching is temporarily replaced by the harmonic potential, and the samples are heated up to about 1000 K before the temperature is gradually decreased to the desired temperature during 1 ns while keeping the force on the ends fixed at 1 nN per chain.

When the molecules are being stretched out, work is done and energy is added to the system through the end-particles. For this reason, it is necessary to use a thermostat that acts locally, and does not regulate the temperature uniformly. The Langevin thermostat is thus the preferred choice rather than the more commonly used Nosé-Hoover. The parameter for the relaxation time in the Langevin thermostat was set to 1 ps.

We stretch the bundles either with constant strain rate, or constant force, corresponding to the experimental conditions of constant strain and constant stress measurements. In the constant strain rate simulations, we increase the separation between the clamps at a constant velocity. In the constant force simulations, the position of the clamps is adjusted to keep the force on the fibre constant at a pre-assigned value. In the simulations with constant strain rate, the force that was applied to a chain before it breaks does not get redistributed over the other chains. This allows us to isolate the interaction between the chains from the interaction mediated by the terminals, which cloud these effects in a system with more realistic boundary conditions. The constant stress condition, on the otherăhand, represents a molecular dynamics realisation of the well known fibre bundleămodel (FBM) with global redistribution of load upon chain breaking.[25] The two modes of operation with constant stress and constant strain rate

Table 2 Force field parameters for the torsion [16]

Torsion [kJ/mol]	$K_{ijk}^{t,0}$	$K_{ijk}^{t,1}$	$K_{ijk}^{t,2}$	$K_{ijk}^{t,3}$	$K_{ijk}^{t,4}$	$K_{ijk}^{t,5}$	$K_{ijk}^{t,6}$
O–C–C–O	2.211	15.194	17.844	-32.460	-13.871	-1.189	12.322
C–C–C–O	5.183	5.610	6.272	-15.428	-0.678	-4.568	3.567

have been carried out with the LAMMPS options `aveforce` and `move` respectively. In one particular sample, torque was added on the atoms on the terminations in the lateral direction with the option `addtorque`. The molecular dynamics simulations have been carried out with finite boundary conditions in all directions.

For the analysis of trajectories, chains are identified as neighbours if the distance between the endpoints on the terminals are less than 1.5 times the estimated bulk separation of the chains, estimated from simulations with 100 chains. Chains with less than six neighbours are counted as part of the contour. Both criteria were validated by visual inspection of the cross sections for a number of bundles.

2.2 Ab initio simulations

Qualitative and quantitative aspects of the breaking of PEO chains at $T = 0$ K have been investigated by density functional (DF) computations. We used the plane wave-pseudopotential formulation of DF theory implemented in CPMD ab-initio simulation package,[26,27] with the exchange-correlation energy given by the generalised gradient approximation of Perdew, Burke and Ernzerhof (PBE).[28]

The system is enclosed in an orthorombic simulation cell with periodic boundary conditions. The plane wave basis of reciprocal lattice vectors is included up to a kinetic energy cut-off of 120 Ry, with the sampling of the Brillouin zone limited to the Γ-point. This last approximation is justified by the large size of the simulation box, and by the insulating character of the material. Only valence states are included in the computation, and the core valence electron interaction is represented by ab-initio norm conserving pseudopotentials of the Troullier-Martins type.[29] Dispersion (van der Waals) interactions are essential to ădescribe lateral chain-chain cohesion. In the present study ăthey are accounted for using the semi-empirical approach by ăGrimme.[30]

In all samples, chains extended along the entire length L_z of the longest side of the periodic orthorhombic simulation cell to mimic an infinitely long polymeric fibre. The periodicity along x and y at $L_x = L_y = 14.4$ Å has been set to keep the lateral interaction of periodic replicas low. Stretching is imposed by increasing L_z beyond its initial value of ~ 3.2 Å per monomer, with the $T = 0$ K condition enforced by minimizing the potential energy by means of quenched MD. Additional DF computations have been carried out on crystalline PEO starting from the experimental structure and unit cell of Ref.[31].

Most computations have been carried out in the spin-compensated picture. Since this might break down in proximity of the bond breaking, a few test computations have been carried out considering unconstrained spin-orbitals, including the possibility of bare spin polarisation in an open shell electronic structure. These tests did not provide any evidence of local spin-uncompensated domain, hence the results reported in the following section all refer to spin compensated computations.

3 Results

3.1 Chemistry of bundle breaking and ab-initio simulations

We begin by investigating in detail the chemistry of bundle breaking, which is however only possible for the smallest bundles, as it requires ab initio simulations. Hence, density functional simulations of stretching and breaking of chains at $T = 0$ K have been carried out on samples made of one and two PEO chains, each chain consisting of 10 -$(CH_2)_2$O- monomers.

3.1.1 Energy versus strain relation

The potential energy per monomer upon stretching a single PEO chain is shown in Fig. 2. A fit of the computational data using the anharmonic functional form:

$$V(\varepsilon) = V_0 + \alpha\varepsilon^2 + \beta\varepsilon^3 + \delta\varepsilon^4 \tag{10}$$

with $\alpha > 0$, where the strain per monomer $\varepsilon = (L_z - L_z^0)/L_z^0$ provides both an estimate of the minimum energy periodicity $L_z^0 = 3.46 \pm 0.05$ Å and an estimate of the potential energy V_0 at periodicity L_z^0. The relatively large uncertainty in L_z^0 is due to a number of reasons. At low strain the potential energy is controlled primarily by weak torsional restoring forces, the energy optimization with respect to the atomic coordinates is slow, the computed potential energy shows small amplitude fluctuations around the minimum, and even the anharmonic fit is not very accurate at negative strain.

To translate V_0 into a binding energy we also computed the ground state energy of the PEO monomer $(CH_2)_2O$ (see Fig. 2). Hence, the computed cohesive energy per monomer $V_c = 103$ kJ/mol in the single chain refers to the ring-opening polymerisation reaction from the ethylene oxide monomer, which is the simplest epoxide ether. Each atom has the same number and type of bonds in the monomer and in the chain, and the relatively low V_c represents the energy gain in releasing the large strain that is apparent in the monomer ground state geometry.

With length increasing beyond L_z^0, the fit of Eq. 10 becomes accurate, and faithfully reproduces the system potential energy up to $\varepsilon = 0.28$. We observe that at low strain ε the dependence of potential energy on ε is remarkably anharmonic, as reflected in the behaviour of $dV(\varepsilon)/d\varepsilon$ reported in Fig. 2, which clearly deviates from Hooke's law in proximity of $\varepsilon = 0$. This is apparently due to the interplay of torsion, bending and stretching energies, whose relative size and role changes progressively with increasing strain.

A linear regime in $dV(\varepsilon)/d\varepsilon$ emerges at intermediate strain $0.04 \leq \varepsilon \leq 0.15$. However, this linear term does not go through

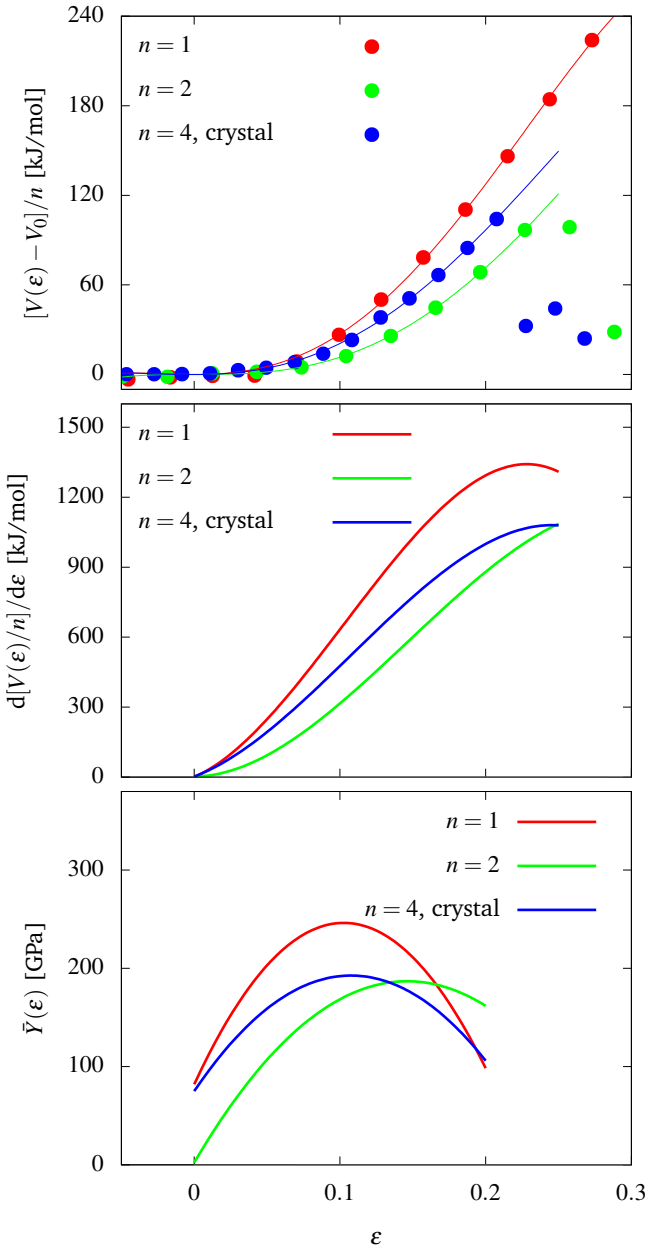

Fig. 2 Top: the potential energy of one and two PEO chains as a function of the strain $\varepsilon = (L_z - L_z^0)/L_z^0$, where L_z is the periodic length corresponding to one PEO monomer per chain and L_z^0 is the deviation from equilibrium at $L_z^0 = 3.46 \pm 0.05$ Å for the single chain; $L_z^0 = 3.26 \pm 0.05$ Å for the double chain; $L_z^0 = 3.27 \pm 0.05$ Å ăfor the crystal sample. The same quantity is reported for the stretching of the PEO crystal cell along the direction of chains, representing the limit of an infinitely extended bundle. Dots: simulation results (DF); full lines: interpolation by the anharmonic fit in Eq. 10. Middle: the stress as a function of the strain, computed by the anharmonic fit in Eq. 10. All energies refer to the single monomer. Bottom: The effective Young's modulus, assuming a cross sectional area of $S = 16$ Å^2 per chain.

the origin as in Hooke's law, but it is given by $dV(\varepsilon)/d\varepsilon = k(L_z^0)^2(\varepsilon - \varepsilon_0)$, with $k = 653$ kJ/(mol Å^2) and $\varepsilon_0 \sim 0.02$. An effective Young's modulus $\bar{Y}(\varepsilon)$ can be estimated from the second derivative $d^2V(\varepsilon)/d\varepsilon^2$, that represents an effective strain dependent force constant $k(\varepsilon)$. To turn $k(\varepsilon)$ into $\bar{Y}(\varepsilon)$, we need to attribute a nominal cross section S to the single chain. This can be done using experimental data on the chain-chain distance ($d = 4.3$ Å) in crystal PEO.[31] Assuming hexagonal cross sections, one obtains $S = 16$ Å^2. Since the force constant depends on ε, also $\bar{Y}(\varepsilon)$ is a function of strain, growing from $\bar{Y}(0) = 82$ GPa at L_z^0 to $\bar{Y}(\varepsilon = 0.1) = 246$ GPa at $L_z = 3.8$ Å /monomer. Both these values are large, with the high-strain value being comparable to steel. Even the highest value can be understood by considering that it refers to the stage of straining dominated by the stretching of C-C and C-O covalent bonds.

It is worth emphasising that this high estimate of the Young's modulus is not directly related to the curvature of the potential energy around its minimum, but corresponds to a high load elastic regime in which a combination of bending and especially stretching energies provide the restoring force opposing further elongation of the chain.

In addition, the stretching process in aligned chains does not correspond to the elastic deformation of a macroscopic PEO sample, in which the averaging over glassy domain and crystal grains of different orientation give origin to a linear (elastic) regime at low strain, of Young's modulus and elastic constants much reduced with respect to the values computed for oriented, defect-free chains.

3.1.2 Structural changes upon stretching

The non-linear dependence of $dV(\varepsilon)/d\varepsilon$ on load is reflected in the strain dependence of the C-C and C-O bond lengths, reported in Fig. 3, of bending angles, shown in Fig. 4, and of dihedral angles shown in Fig. 5. The plots confirm that, as expected, dihedral angles are the first to manifest sizable strain, followed by bending, and stretching in the last stage. The MD results for the bond lengths match the DFT results over the entire range. The angles are shifted by about 3 to 4 degrees in the range we are interested in but otherwise also show similar behaviour as well. Only the torsional angles show significant quantitative deviation between MD and DFT calculations. This could be related to a shift in the hybridisation of the C atoms (see below), which is not captured in the classical force field. Regardless, the high-strain behaviour is dominated by bending and stretching, and therefore this difference will likely not have a qualitative effect on the behaviour at high strain, which is what we focus on in this work.

Deviation of the applied force from the linear behaviour at $\varepsilon > 0.19$ corresponds to the onset of high-strain anharmonicity, which dominates the system behaviour in the last stages of stretching. The applied force reaches its maximum at $\varepsilon = 0.22$. Beyond that length, the force decreases with increasing strain, and the system would be unstable under constant stress conditions. If subjected to thermal fluctuations at non-zero temperature, it would break even earlier. The clearest signature of breaking appears in the strain dependence of bond lengths. More in detail, the strain dependence of C-C and C-O is non-monotonic at first, then both

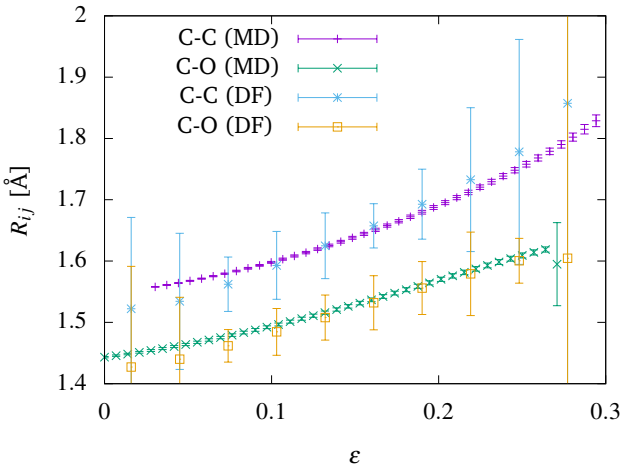

Fig. 3 Bond distances during the stretching of a single PEO chain computed by GGA-DFT and MD.

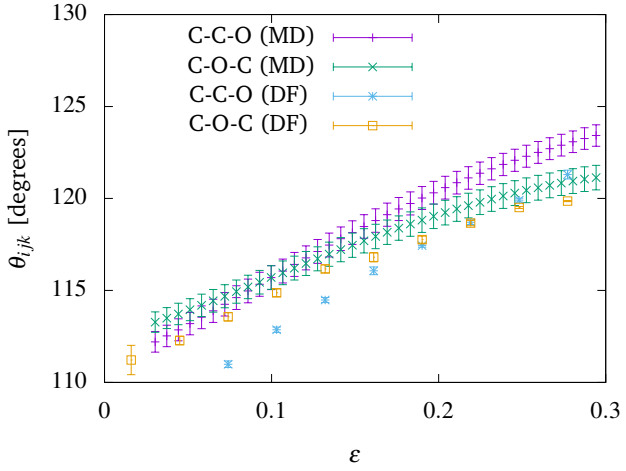

Fig. 4 Bending angles during the stretching of a single PEO chain computed by GGA-DFT and MD.

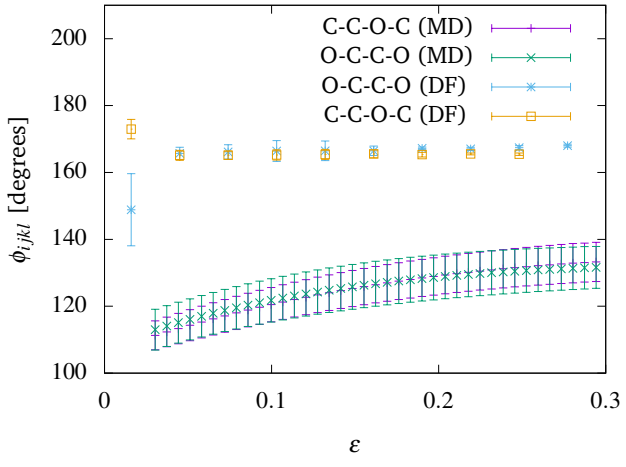

Fig. 5 Torsional angles during the stretching of a single PEO chain computed by GGA-DFT and MD.

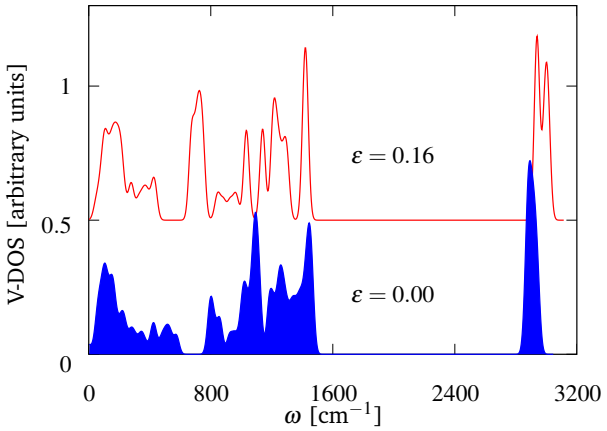

Fig. 6 Comparison of the vibrational density of states (V-DOS) computed by DF at two different values of the longitudinal periodicity: $\varepsilon = 0.00$ (blue line) and $\varepsilon = 0.16$ (red line).

bond lengths increase linearly for $0.04 \leq \varepsilon \leq 0.2$,with a relative variation larger for the C-C than for the C-O bond length. Non-linearity in the strain dependence of the bond lengths appears at $\varepsilon \sim 0.23$. Above this length the slope of C-C with strain turns upwards, indicating the incipient failing of C-C bonds. Anharmonicity of the restoring force and non-linearity of bond lengths versus strain are fully developed at $\varepsilon \sim 0.26$, an elongation at which the single chain appears broken at several C-C bonds even by visual inspection of simulation snapshots. Remarkably, the trend shown by C-O over the same range of global strain is opposite, since C-O saturates at a fairly high value while C-C increases rapidly.

An interesting view of the same breaking process is obtained by looking at the standard deviation along the chain of individual bond lengths, shown in the error bars of Fig. 3. The minimisation of the chain energy in the anharmonic regime at low strain makes bonds slightly inequivalent from each other despite connecting the same type of atom. Thus, the standard deviation σ of chemically equivalent bond lengths is not negligible at low strain. Then, σ decreases with increasing strain, since restoring forces become stronger, making bond lengths better defined. Eventually, σ shows a rapid and drastic increase above $\varepsilon = 0.23$, providing the most unambiguous sign of chain breaking.

The spread of C-C bond lengths leading to breaking could be reflected in spectroscopic data. To highlight this effect, we computed by DFT the vibrational density of states of the single PEO chain at three different values of the longitudinal periodicity, corresponding to $\varepsilon = 0$, $\varepsilon = 0.16$ and $\varepsilon =$ and $\varepsilon = 0.25$. At the near-equilibrium periodicity of $\varepsilon = 0$, the vibrational density of states shows the typical features of similar organic systems, with a high frequency band at $2800 \leq \omega \leq 3100$ cm^{-1} due to the C-H bond stretching, an intermediate band due to bond bending at $1200 \leq \omega \leq 1600$ cm^{-1}, and a broad background of modes at $0 \leq \omega \leq 1200$ cm^{-1}, of mixed character but consisting primarily of bond-torsion modes (See Fig. 6). With increasing strain, the C-H stretching band moves to somewhat higher frequency and splits into a symmetric (at the highest frequency) and an anti-symmetric (at slightly lower frequency) C-H stretching. Bend-

ing modes move to slightly lower frequency, while the range at $\omega \leq 1200$ cm^{-1} shows the major and least predictable changes, that could easily be detected by spectroscopy and could be used to monitor the system evolution up to near breaking conditions. The chain breaking itself, taking place at $\varepsilon = 0.23$, is likely to be a stage too short to be characterised by spectroscopy. Moreover, the changes in the vibrational DOS upon breaking are less easy to predict and to interpret, since new molecular species appear in the system, possibly spin-unpaired radicals, not easily accounted for even at the DF-level.

Notice that with increasing strain bending angles tend to 120° and dihedral angles tend to 180°, values that characterise organic structures of sp^2 bonding. Since bonding angles modulate the size of Hamiltonian matrix elements, their correspondence with the sp^2 geometry suggests that the sp^3 bonding of the unstrained chain turns to sp^2 at high strain. The change of electronic structure with increasing strain is supported by the computation of atomic charges, evaluated by the electrostatic potential (ESP) method.[32] The results show an enhancement of atomic charges with increasing strain, followed by a sudden drop at breaking. These effects are not accounted for by standard reactive classical force fields, such as ReaxFF.[21]

As already stated, the single PEO chain does not collapse upon crossing the length corresponding to the maximum restoring force. In other words, the chain does not snap during simulated breaking, because of the constant strain condition enforced by these DF simulations, and of the absence of lateral perturbations from thermal fluctuations that could undermine the strained geometry in its metastable regime. Moreover, no simple healing process is available to the single chain, which splits in a collection of geometrically equivalent strained epoxy units. In reality, it might be practically impossible to maintain (meta)-stability beyond the linear stages, at $\varepsilon > 0.19$.

3.1.3 The two-chains system

To assess the role of chain-chain interactions the simulation of stretching at $T = 0$ K has been repeated for a sample consisting of two chains. The effect of these interactions turns out to be sizable, and, surprisingly, it has the effect of decreasing the strength of the bundle under tensile load.

Also in this case, strain has been imposed by changing the periodicity of the unit cell containing 2×10 PEO monomers. As before, for any given periodicity, the potential energy $V(\varepsilon)$ has been carefully optimised with respect to the atomic positions by quenched molecular dynamics, and the resulting $V(\varepsilon)$ has been fitted by the same expression of Eq. 10. The length of minimum potential energy turns out to be $L_z^0 = 3.26$ Å , i.e., nearly 0.2 Å shorter than for a single chain. This could be due to the effect of the surface tension (surface energy, at $T = 0$ K) *per unit length* of the bundle, which is stronger for two chains than for one, and tends to reduce the surface area and thus the length of the system.

Comparison of the ground state energy of the single and doubleăPEO chain computed at the DF level allows us to estimate the chain-chain cohesive energy of two chains at 1.2 kJ/mol per PEO monomer. A similar comparison for the crystal sample gives a cohesive energyăof 13.1 kJ/mol per PEO monomer. ăWe emphasise

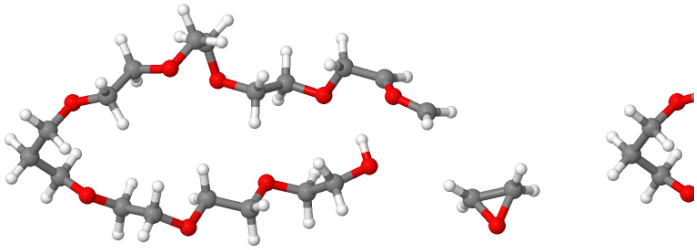

Fig. 7 Partial healing of the broken two-chain bundle.

that this cohesive energy arises from the chain-chainăinteraction, due to dispersion energy only, and without any ăreference to the energy gained in forming chains from theăepoxide monomer.

With increasing strain the evolution of $V(\varepsilon)$ (shown in Fig. 2) qualitatively follows the same behaviour of the one-chain case. The computation of dihedral angles, bending angles and bond stretching shows that also these structural parameters follow the same trends in both cases, consisting at first in the deformation of dihedral angles, then of bending angles and finally of stretching bond distances. A quantitative comparison is not easy, because of the different reference length L_z^0 of the two samples. It is apparent, however, that the two-chains system breaks at a shorter length and at a lower applied force per chain than in the single chain case. In the case of two chains, the apparent Young's modulus computed from $\mathrm{d}^2V(\varepsilon)/\mathrm{d}\varepsilon^2$ depends on strain, starting from about 2 GPa at low strain, and reaching 183 GPa at high strain.

Analysis of configurations shows that the monomers in the two chains never really align in the lateral direction, confirming the sizable role of chain-chain interactions. These interactions are apparently amplified by the helicity of each PEO chain, adding a longitudinal modulation of short-range repulsive interactions in addition to the attractive dispersion forces. The longitudinal corrugation in the interaction energy, in particular, gives rise to multiple local minima in the potential energy, that make it difficult to unambiguously identify the ground state of bundles.

3.1.4 Chemical rebonding after chain breaking

Ab-initio computations offer a glimpse of the events following the breaking of individual chains in the two-chains system. We find that at first, the separation of one chain into nearly equivalent segments is observed, terminated by planar OCH_2 groups, in which C is in the sp^2 electronic configuration. Then, interaction with the neighbouring chain causes the collapse of the bundle, with a short sequence of chemical changes that carry out the partial healing of the broken two-chains bundle as displayed in Fig. 7. At long times, the healing results in finite chains terminated by OH on one side, and planar OCH_2 on the other side, with the release of a few epoxide ether monomers. The post-breaking evolution given by DF computations might be affected by limitations of the approximate DF approach in tackling open shell species, and, in any case, it is not correctly reproduced by the classical force field model, even at the qualitative level. Perhaps it might be described by some highly sophisticated reactive force field models, that, however, require heavy stages of parametrisation.

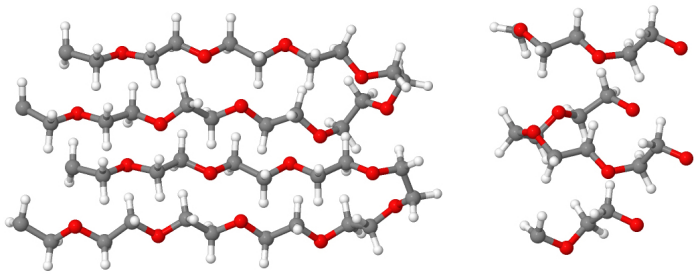

Fig. 8 Final state upon stretching a crystal sample up to the breaking point. The system has been rotated along the long axis to expose chains that otherwise are partially hidden in the trapezoidal cross section. Healing takes place by connecting neighboring chains forming loops returning to a single clamp. One of the chains appears to be broken because of periodic boundary conditions.

3.1.5 Stretching crystalline PEO

To assess the effect of helicity of PEO chains and of lateral chain-chain interactions, simulations have been carried out for the experimental crystal structure of PEO, in which chains are closely packed. In our study, the periodic system is seen as the limiting case of thick bundles. The apparent effect of the condensed environment is to give a complex unit cell, containing four chains and 28 monomers in total, with an average equilibrium length per monomer of 3.27 Å.

Especially at low strain, the $V(L_z)$ curve (see. Fig. 2) for the extended system shows a fine structure, apparently due to the lateral interactions, creating conditions of local minima and sometimes preventing a complete energy optimisation. Nevertheless, the energy increase with increasing periodicity at low strain is more parabolic than in the single and double chain case, since in the condensed phase it is more difficult to decouple torsion, bending and stretching than in the few-chain samples. As a result, the apparent Young's modulus $\bar{Y}$ computed from the strain-dependent force constant is somewhat more constant than in the one- and two-chain cases, varying from $\bar{Y} = 75$ GPa at low strain to $\bar{Y} = 190$ GPa at intermediate strain. The bundle breaks at shorter periodicity per monomer ($L_z = 3.7$ Å) than the one and two-chain system. Also in this case, the breaking of one chain destabilises neighboring chains, giving rise to chemical reactions. The healing of broken bonds is complete, giving rise to a set of loops breaking the continuous connection between the two sides of the broken bundle, without leaving behind any radical species as shown in Fig. 8.

As a result of the healing process, the final potential energy per monomer is only 3.2 kJ/mol higher than the ground state energy. The low energy of the final state emphasises the fact that bundles become metastable very soon upon stretching, and only the kinetic barrier encountered by the healing process prevents the breaking at much lower strains and stresses than found in the simulation. The argument is even more compelling for thick bundles, in which healing might occur by reacting with neighboring chains, and for long bundles, since the energy required for a given relative stretching is extensive, and the energy required to break a chain is a constant.

There are obviously many things in the chemistry of the chains that are not captured by the classical force field. The most important among them is the fast chemical rebonding of chains following their breaking under strain, effectively removing all dangling bonds from the system. However, from comparing the behaviour of the bond stretching and bending at high strain, we conclude that the classical force field captures the behaviour of the chain under high strain sufficiently well up to the breaking point.

3.2 Stretched bundles with $N > 2$ chains

We continue by investigating the structural properties of stretched bundles of up to 24 chains, now using molecular-dynamics simulations and potential energy minimisation based on the empirical force field described above. At any non-vanishing temperature, entropy effects turn unconstrained chains into coils, whose radius scales like the square root of the number of monomers N. In addition, there are finite-size effects and bead-bead, i.e. non-bonded, interactions which cause deviations from the ideal scaling. In our systems, the clamps and the tension applied to the bundle change the picture qualitatively and quantitatively. An example of a stretched bundle at finite temperature is shown in Fig. 1.

3.2.1 Structure at low and vanishing temperature

To give a first characterisation of structural, cohesive and elastic properties of PEO bundles, and to provide a term of comparison for the results of MD simulations to the DF simulations, we first investigate the bundles in the limit of very low temperature and under moderate tensile load ($\kappa = 1$ nN per chain), an order of magnitude below the breaking limit. At low temperature T this *moderate* tension is sufficient to force the bundles chains into approximatively linear configurations.

Once chains adopt the linear configuration, the bundle structure is determined mainly by the geometry of its cross section, that can be visualised as a 2D cluster, in which the interaction among particles is represented by the integral along z of the lateral chain-chain potential energy. The full 3D system, however, is more complex due to the nonisotropic lateral interactions.

To approach the $T = 0$ K condition, the energy of N-chain bundles is first minimised with respect to all coordinates (at fixed applied force) by short annealing runs of 1 ns. These cannot guarantee that the simulation will reach the ground state of the system, but the relatively ordered geometry of samples up to at least room temperature suggests that the potential-energy landscape consists of only a few major valleys, and the geometries determined by short annealings are likely to be representative of low temperature structures, providing information also on defects and isomers.

The sequence of clusters obtained in this way is reported in Fig. 9. As already stated, in this figure all bundles are under a 1 nN/chain tensile load. Once again, as expected, the compact hexagonal motif dominates the structure of the 2D clusters. However, non optimal geometries arise because of short annealing and incomplete optimisation. Moreover and more importantly, both unexpected 2D geometries and longitudinal variations in the cross section arise from the spontaneous helicity of PEO chains, which adds a small but complex perturbation to the lateral interactions.

An example of nearly degenerate isomers in the 2D cluster

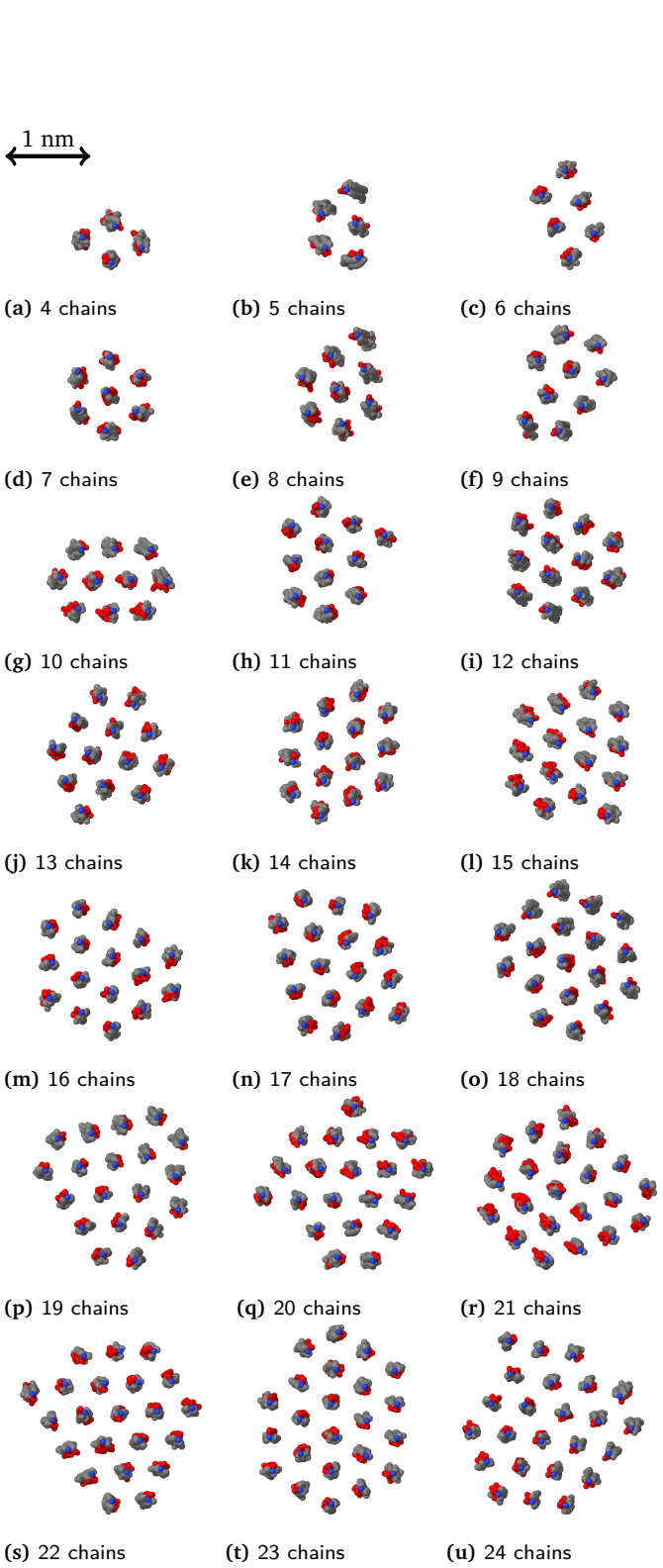

Fig. 9 Cross sections of bundles of sizes from $N = 4$ to $N = 24$ at $T = 0$ K with a constant force of 1 nN per chain.

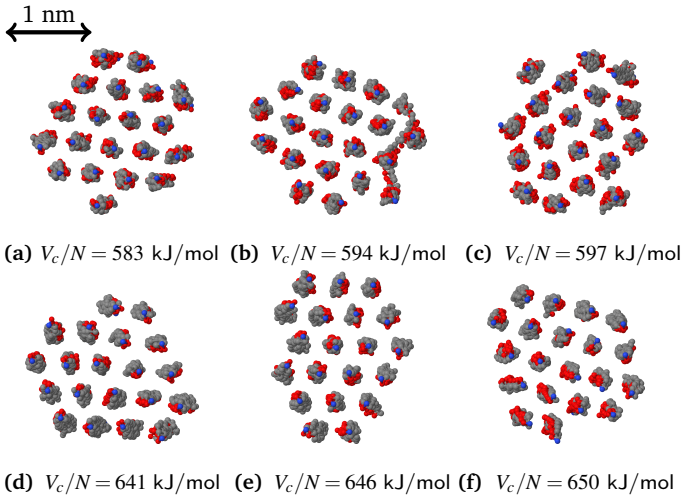

Fig. 10 Isomers of the 2D cluster representing the structure of the 20-chain bundle at $T = 400$ K with a constant force of 1 nN per chain obtained by equivalent optimisation cycles started from independent configurations. The cohesive energy per chain associated with each configuration averaged over 2 ns is given in the sub-caption. Fig. (a)-(c) represent low cohesive energy configurations, and (d)-(f) represent configurations with high cohesive energy.

representation, corresponding to different bundle polymorphs, is provided by the structure of the 20-chain bundle (see Fig. 10), found in several different configurations as a result of successive fast optimisation cycles. The cross section may also change along z, when one or more chains are not quite straight, but show a marked winding around some other chain as seen in Fig. 10 (b).

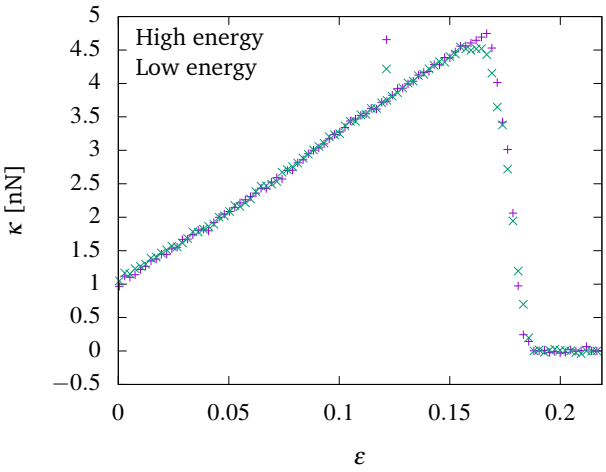

Fig. 11 Force elongation curves averaged over the three high energy configurations showed in Fig. 10 (a)-(c) and for the low energy configuration showed in Fig. 10 (d)-(f).

Fig. 11 shows the average force-elongation curves for the three high-energy isomers shown in Fig. 10 (a)-(c), and for the three low-energy isomers shown in Fig. 10 (d)-(f). The initial slope is the same, but the high-energy isomers are able to sustain a little more force than the low-energy ones. This observation is reminis-

cent of mechanical hardening in metals. However, the two effects are not obviously related, since hardening in metals is caused by defects blocking the movement of dislocations, while in our system dislocation dynamics does not play an obvious role in the yield. It is thus not clear what is the origin of this effect, whose magnitude, in any case, is apparently quite small.

The ideal, regular-looking cross-section is not always the one with the lowest energy. In several cases, the atomistic bundles of N chains adopt a cross-section different from the one in the ideal sequence, contradicting the assumptions of cylindrically symmetry and invariance along z. We found that this difference is often not the result of incomplete optimisation of the atomistic bundles, since preparing them according to the ideal cylindrical cross section almost invariably results in a higher potential energy. Structures of this type clearly point to the effect of the PEO chain helicity on the geometry of bundles.

The plot of the cohesive energy per chain in the lowest energy structure for each N displays the characteristic trend found in the size dependence of cohesive energies for atomic and molecular clusters. Cohesive energy increases rapidly at first, and then saturates slowly to the cohesive energy per chain of a hexagonal arrangement of linear and aligned chains. The shortfall of cohesive energy at low N can be attributed to the surface energy, whose fractional weight on the total cohesion is highest for $N = 1$, and decreases as $\sqrt{N}$ with increasing size.

To leading order, the energy of the bundle can be estimated from the volume and the surface area, i.e. the compact surface delimiting the bundle. First, we quantify the surface area, or equivalently, the perimeter of the 2D cluster. To this aim, we attribute an hexagonal cross area to each chain in the bundle, with an inter-chain distance $d = 4.3$ Å . Then, the perimeter C_N of the 2D cluster is determined by counting the number of hexagon sides exposed to the vacuum. The size dependence of the cohesive energy of the bundle is represented as:

$$V_c(N) = NV_0 - \sigma C \tag{11}$$

where V_0 and σ represent the bulk energy per chain and the surface energy, respectively, to be determined by fitting the numerical values of the cohesive energy. Since, on average, the contour length scales as $C \propto N^{1/2}$, we recover the expected scaling of the cohesive energy per chain:

$$\frac{V_c(N)}{N} = V_0 - \alpha \frac{\sigma}{N^{1/2}} \tag{12}$$

where the numerical coefficient gives the (average) proportionality of C_N and $N^{1/2}$

Comparison of the computed $V_c(N)$ with the result of the smooth fit in Eq. 12 shows a good match, as seen in Fig. 12. The single sample with $N = 100$ had $V_c/N = 760$ kJ/mol after 1 ns of annealing, which is about 2% higher than the prediction given by the fit for $T = 300$ K in Eq. 12. To investigate the impact of the annealing time, the annealing procedure was repeated with an additional 2 ns of annealing time, which increased the cohesive energy by about 3%. While longer annealing times indeed results in lower energy structures, 1 ns is considered to give a reasonable

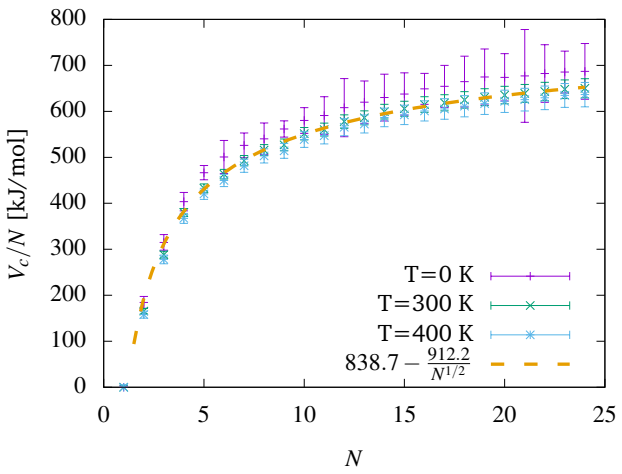

Fig. 12 Computed cohesive energy per chain as a function of size N at $T = 0, 300, 400$ K, with a fit by the smooth expression in Eq. 12, representing the interplay of bulk cohesion and surface energy.

balance of realism and efficiency.

The N and $\sqrt{N}$ scaling of cohesive energy is less apparent in the average bundle length $L(N)$ measured by the separation of the clamps and Young's modulus at non-zero temperature, as we will see in the next section 3.2.2. In these cases, we see a sequence of peaks and dips, that point to sizes whose packing exposes an optimal or unfavored contour, respectively. The single sample with $N = 100$ at $T = 300$ K had a length of $L = 114.6$ Å after the first annealing run of 1 ns, and a length of $L = 114.7$ Å after an additional annealing run of 2 ns, which is about 0.2% lower than expected from the smaller systems.

At $T = 0$ K we determine the relation of length L_z and stress by increasing L_z in regular steps, and minimizing the potential energy at each step with respect to all internal degrees of freedom. Stress κ is computed from the forces on the terminals. The Young's modulus for the breaking of a single chain was calculated from the slope of the beginning of the strain curve to be 144 ± 6 GPa, again assigning the chain a cross sectional area of $S = 16$ Å^2.

Breaking at $T = 0$ K takes place in a localised way, focusing strain on a limited stretch of the chain when the system crosses the stability boundary. At $T = 0$ K, the pictures of breaking at constant stress or constant strain are equivalent. However, these two modes of stretching differ in very important aspects at non-zero T, because of the role of fluctuation and thermal activation.

3.2.2 Nonzero temperature

At finite temperature, we use the simulated annealing protocol described in Sec. 2 at the desired temperature, to obtain equilibrium conditions at a constant applied force per chain. Typical cross-sections of the bundles obtained in this way are shown in Fig. 13. The figure shows that the hexagonal structure observed at low temperature remains highly ordered even at high temperatures. When the number of chains in a bundle has specific values (such as 3, 7, or 19), a shape of minimal contour forms with complete shells. However, when the number of chains is not one of these "magic" numbers, then there are typically several possible

isomers appearing. Nevertheless, the hexagonal lattice structure usually remains. We have observed one special case, for $N = 22$, where we have found a 7-fold symmetric bundle with full shells. In extended 2D lattices, such defects have to be coupled to a 5-fold symmetry defect, forming the two end points of a dislocation line. In finite systems, one of the two conjugated defects may be annihilated at the surface. Sometimes, but especially if we do not anneal the system and instead run it at constant temperature, we find a more disordered state, where the isomerisation changes along the length of the bundle. We have also observed that isomerisation can also change with time.

The lengths of the bundles at $T = 300$ and 400 K with a constant applied force per chain of 1nN is shown in Fig. 14. For comparison, a single chain at $T = 0$ K had a significantly longer length of 115.7 ± 0.1 Å. The length depends only weakly on the size of the bundle and levels off quickly for bundles consisting of more than 20 chains. For small bundles, there is a clear signature of the "magic" numbers at 3 and 7, but for larger bundles this effect is smaller and washed out by statistical error and thermal noise. Overall, the effect of the bundle size is significant, but small. The cohesive energies show even less of the structure (see Fig. 12). At this strain, the entropic effects are small, which is evident from the weak temperature dependence of both the average length and the Young's modulus. The general trend is the same as for the *ab-initio* computations presented in section 3.1 in that the equilibrium length is shorter with increasing bundle size. This can be seen clearly in Fig. 15, where the average length at which the first chain in the bundle breaks is shown as a function of bundle size. For the bundle with 100 chains at $T = 300$ K the first chain broke at a length of $L = 134.8$ Å, in good agreement with the picture from Fig. 15.

The force per chain as a function of strain is shown in Fig. 16 for a number of different-sized bundles at various temperatures. For all sizes, there is an initial linear elastic regime. The force remains almost linear in the strain until the first chain in the bundle breaks.

The Young's modulus can be computed from the slope of $\kappa(L)$ at low strain. Here it was estimated by linear regression up to a strain of 0.05, about 30% of the strain at which the first chain breaks. The resulting Young's moduli are presented Fig. 17. The modulus display no significant size dependence for systems of size $N > 9$, also the bundle of 100 chains at $T = 300$ K had a Young's modulus of $Y = 130$ GPa. Experiments with Linear PE also indicate that the Young's modulus to a good first approximation is independent of the molecular weight, as the macroscopic deformation is the dominant factor.[33] In agreement with previous findings[34], one can see that a decrease in temperature will lead to an increase in the modulus.

The estimated modulus is high. The experimental values for the Young's modulus of bulk PEO is typically on the order of 0.1-20 MPa.[35–37] Though the Young's modulus and the tensile strength of these amorphous samples are not determined by the stretching of covelent bonds, but rather by weaker interactions.[38] For the elastic properties of PEO along the chain axis, an experimental value of 10 GPa has been reported,[39] in well agreement with computational results.[9] The values we find from our simulations for

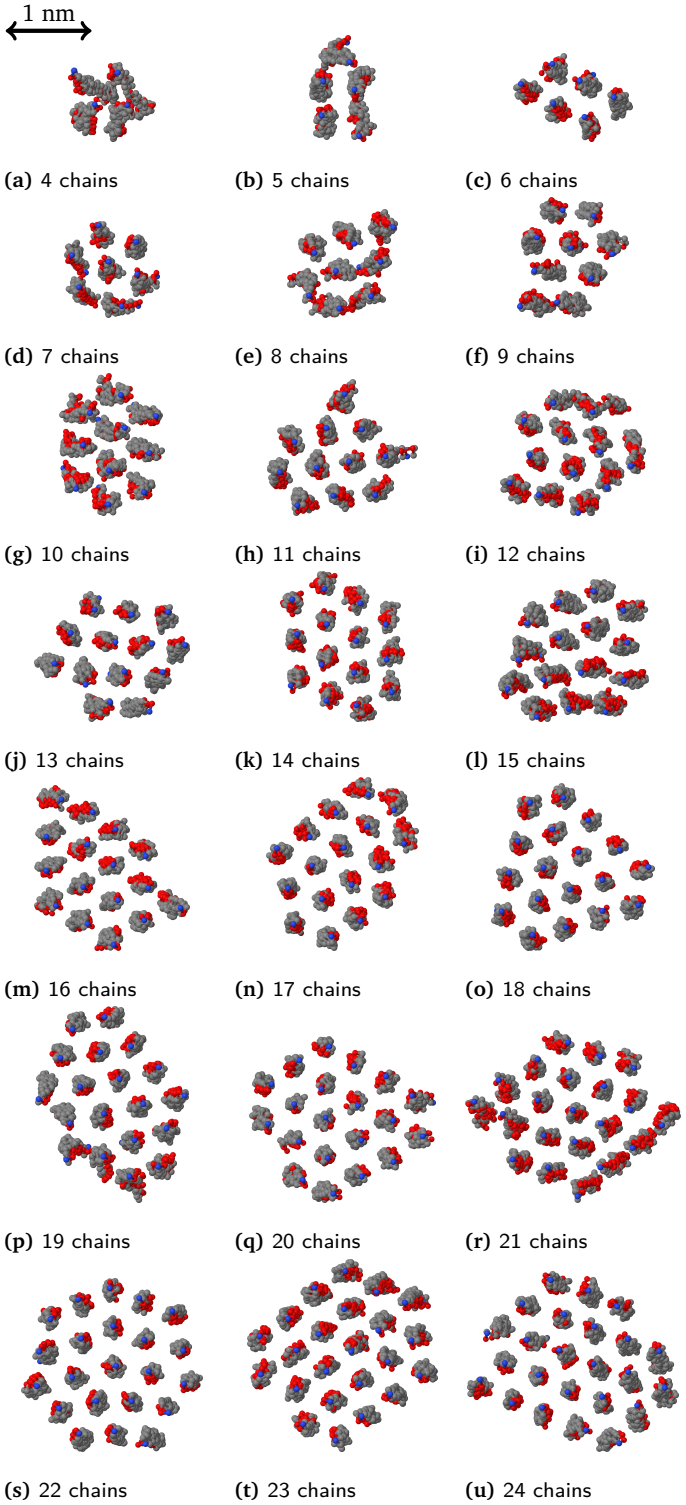

Fig. 13 Cross sections of bundles of sizes from $N = 4$ to $N = 24$ at $T = 400$ K with a constant force of 1 nN per chain.

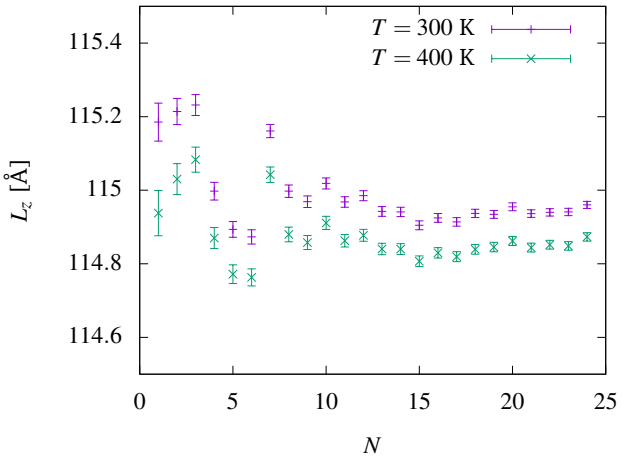

Fig. 14 Average bundle length $L(N)$ for 100 samples as a function of size N with a constant force of 1 nN per chain at $T = 300$ K and $T = 400$ K.

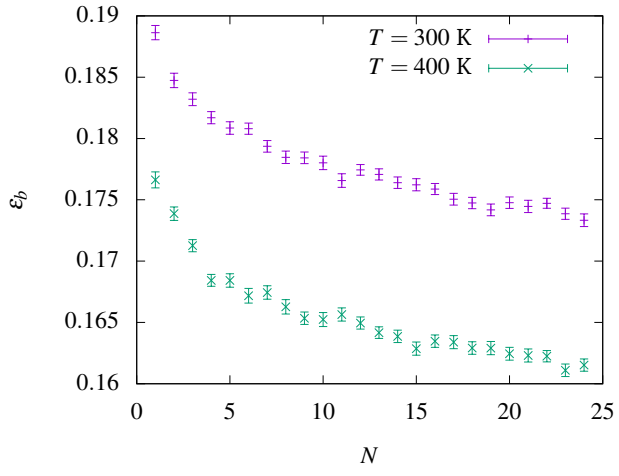

Fig. 15 The average strain at which the first chain in the bundle breaks, indicated as ε_b, for 100 samples at constant strain rate 0.8 m/s as a function of size N at $T = 300$ and $T = 400$ K.

PEO are much higher, comparable to the values for PE.[40] Stretching of thermoplastic PE gives a Young's modulus on the order of 1 GPa,[41] while experiments with single crystals gives a modulus in the range 168-278 GPa,[42,43] and even up to 370 GPa for low density films.[39] Ab-initio computations of single chain PE gives a modulus between 300 and 500 GPa.[10,34,44]

We can understand this by considering that the stretching constants of bulk PEO in experiments is strongly determined by the structure. A major difference between PE and PEO is that the latter is known to have a loosely coiled confirmation.[9] The high modulus and high strength found in fibers relies mainly on high polymer chain orientation and extension, and polymers with helical chain configuration exhibit a much lower theoretical modulus[45]. In our model the chains are extremely extended and ordered, producing systems far from the complexity of macroscopic samples. Our semi-crystalline fibers resemble more closely the structure of PE, and thus display similar mechanical properties.

3.3 Breaking

We now turn to the further stretching and finally breaking of the larger bundles in the classical molecular-dynamics simulations. We discuss here the results of simulations at a constant strain rate, stretching out the bundles, until all the chains have broken. Figure 18 shows a sequence of snapshots of a bundle of 17 chains being stretched out and breaking.

The computational limiting resistance load κ_l was estimated from the average curves in Fig. 16 to 30.5 ± 0.1 GPa at 300 K 28.4 ± 0.1 GPa at 400 K. For 0 K, κ_l was estimated to 36.9 ± 0.3 GPa using the same methodology with 10 samples of single chain bundles.

Because our simulations are at constant strain rate, the force that was applied to a chain before it breaks does not get redistributed over the other chains. This allows us to isolate the interaction between the chains from the interaction mediated by the terminals, which cloud these effects in a system with more realistic boundary conditions. If there were no relevant interaction between the chains, then each chain would break independently, and the fraction of broken chains would not depend on the bundle size. We observe only a small systematic size dependence.

There are several important further observations that can be made regarding the dependence of breaking on temperature and bundle size.

3.3.1 Thermally activated breaking

At higher temperature, the chains are slighly shorter and the Young's Modulus is lower, in agreement with previous findings from DF simulations of crystaline polyethylene.[34] Also, chains break earlier and breaking times follow a broader distribution. Ideally, neglecting the weak lateral interaction, at $T = 0$ K, all chains break at the same length.

The breaking rate of chains from the simulations is shown in Fig. 19. The spread of breaking times and earlier breaking can both be understood from thermal activation. Before the zero-temperature breaking point is reached, the chains can break by thermal fluctuations. At higher temperature, there are more and bigger thermal fluctuations, and hence the chains may break more

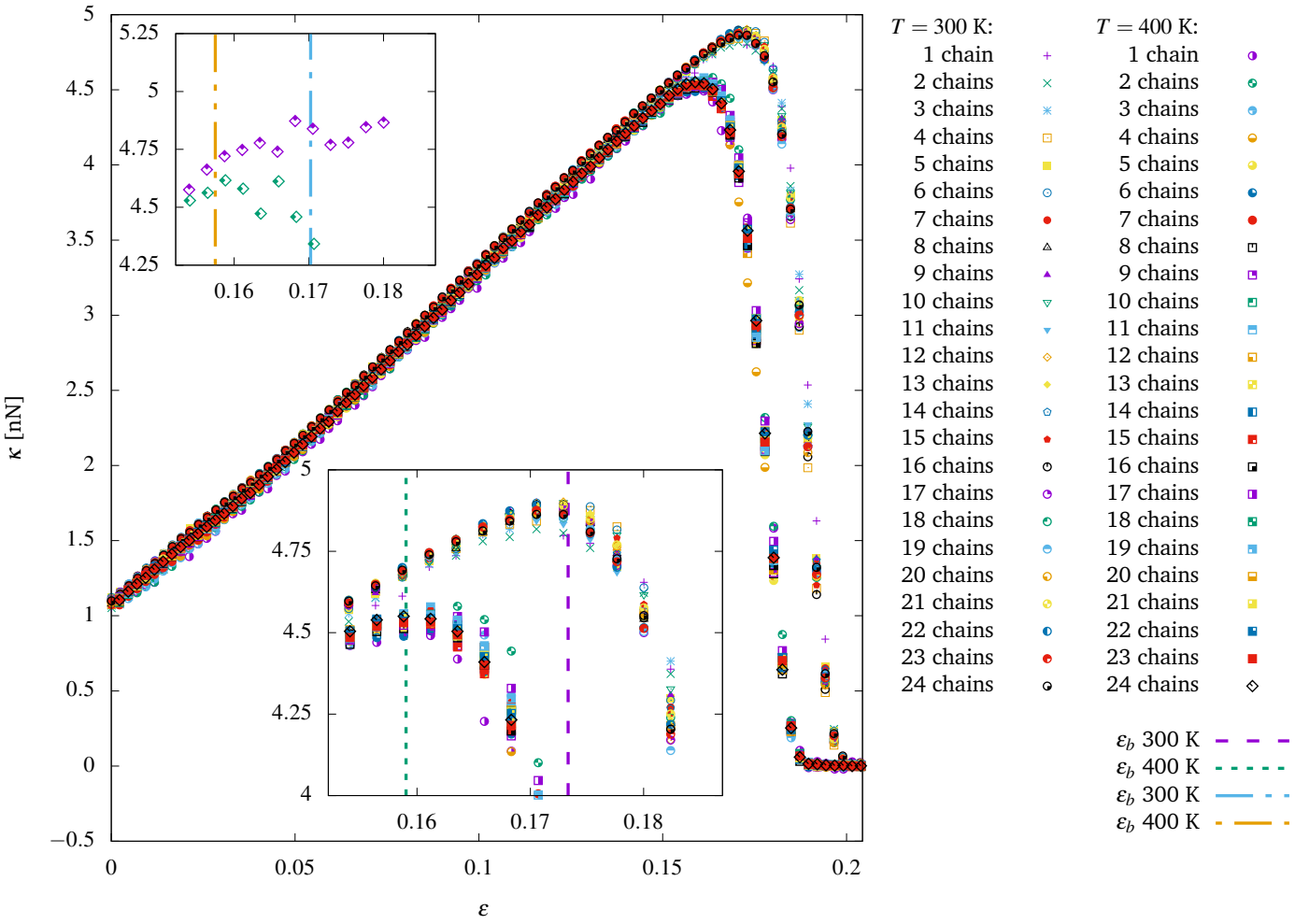

Fig. 16 The force per chain during constant strain rate simulations at 0.8 m/s for system of bundles of $1-24$ chains of at $T = 300$ K and $T = 400$ K. The lower inset shows the breaking part zoomed in, with lines indicating when the first chain broke on average in bundles of size $N = 24$, labeled as ε_b. The upper inlet shows single samples with bundles of size $N = 24$, and again the lines indicate when the first chain in the bundle breaks.

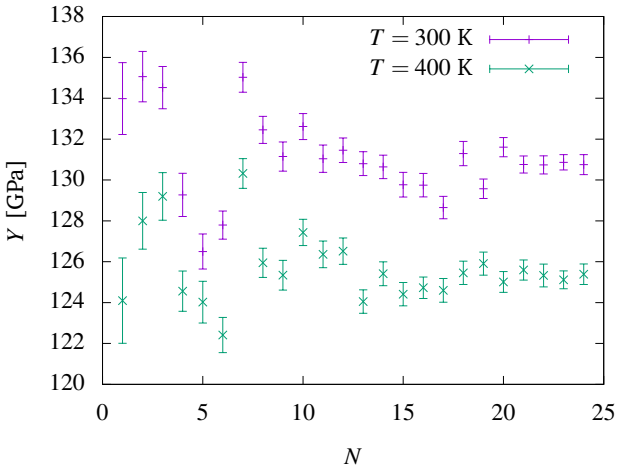

Fig. 17 The Young's modulus of bundles of PEO with a constant strain rate of 0.8 m/s as a function of size N at $T = 300$ and $T = 400$ K. The Young's modulus are estimated from the strain curves, with 100 samples per system.

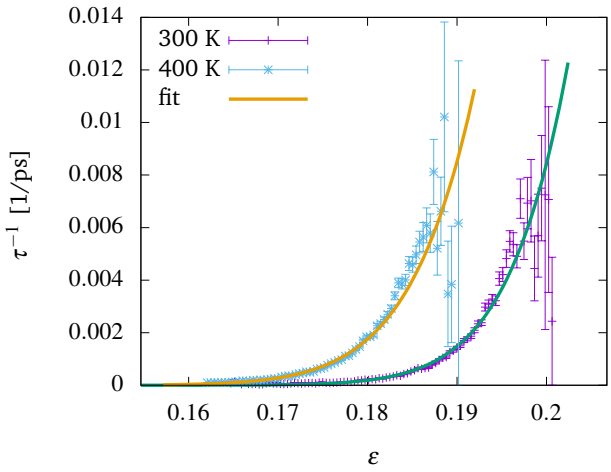

Fig. 19 The rate of chains breaking as a function of strain, for temperatures $T = 300$ and $T = 400$ K averaged over bundles of size 16-24 chains with 100 samples each. A fit using the expression for one-dimensional thermally activated breaking, Eq. 15, is also included.

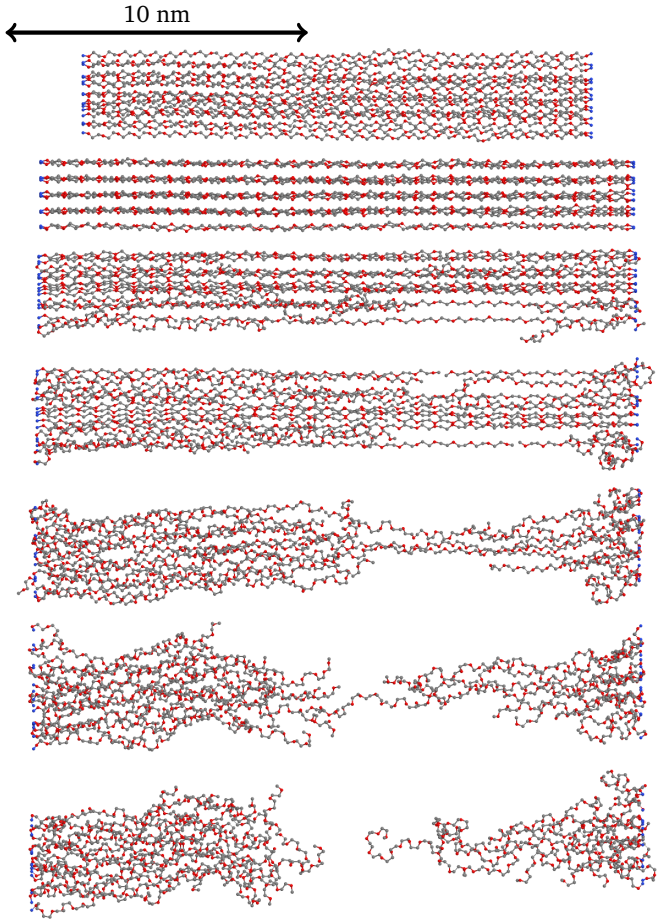

Fig. 18 Snapshots of a bundle of 17 chains under a constant strain rate of 0.8 m/s, stretching out and breaking at $T = 400$ K.

quickly. The activation free energy depends on the strain. At low strain rates, it takes more time for thermal fluctuations to overcome the higher barrier.

We can make some simple estimates of the thermally activated breaking rate and dependence on strain rate and temperature. For this purpose, we treat the chain as one-dimensional and assume that the chain-chain interaction is negligeable. We assume that each breaking bond experiences a mean field response from the rest of the chain equal to the average force in the chain, F_0. The total potential-energy landscape then consists of a linear term and the energy of the bond. For small forces, there is a deep minimum for the intact bond and an even deeper escape with a broken bond, with a high barrier inbetween. For some critical force F_c this minimum completely disappears at r_c, and even at $T = 0$ K the bond would break without any thermal activation. When a bond breaks through thermal activiation, it can be assumed to be close to this point and thus F_0 is close to F_c.

We expand the potential-energy landscape around the breaking point r_c to the third order, and locate the nearest maximum and minimum at a distance close to the breaking point,

$$\Delta r = \sqrt{\frac{\Delta F}{3C_3}}\,, \tag{13}$$

where $\Delta F = F_0 - F_c$ and C_3 is the third order expansion coefficient. We can then obtain the escape rate from the Kramers rate given by

$$\tau^{-1} = \frac{\Omega^2}{2\pi\gamma}\exp\left[-\Delta E/(k_B T)\right] \tag{14}$$

with Ω being the instantaneous effective oscillation frequency, ΔE being the energy barrier and γ the microscopic friction coefficient (viscous). We find

$$\tau^{-1} = C\Delta r \exp(-6C_3\Delta r^3/(k_B T))\,, \tag{15}$$

with C a constant. This result contains several parameters that

depend on the details of the complex potential landscape and dynamics, which we must obtain indirectly through fitting.

A fit of Eq. 15 to the simulation results is included in Fig. 19. The expression fits well, but we note one odd result in the fit parameters. The value found for the parameter r_c, 151.9 ± 0.2 Å, the length at which a break is immediate, is higher than the breaking length found in the 0 K simulations, 147.1 ± 0.2 Å for a single chain. This is probably related to the fact that the real energy landscape is much more complicated than in our simple 1D estimate, and there are several different reaction paths that may be activated at different temperatures. We have also briefly tested the dependence on the strain rate, and found that it behaves as expected: At higher strain rate, the chains break at a higher strain. The breaking rate, however, is not dependent on the strain rate, which implies that we are indeed in the adiabatic regime.

3.3.2 Bundle size and structure

We have investigated the dependence of various observables on the size of the bundle. Neglecting lateral chain-chain interactions, the force versus strain curve would be the same for all sizes. Simulation results, however, show that the force per chain for bundles of different sizes do not fall exactly on top of each other, but are quite close. This observation points to the effects of chain-chain interactions, which are small but not completely negligible, as already suggested for the results for the linear regime and for the Young's Modulus.

To deepen our understanding of the bundle effect on chain breaking, we examine the location of the first bond that breaks inside the bundle. As seen in section 3.1, the C-C bonds are weaker than the C-O bonds, and are therefore more likely to break. At $T = 300$ K, 94.8% of the first bonds to break in each chain are C-C bonds. This strengthens the connection to PE mentioned in Sec. 3.2.2. At $T = 400$ K, 87.4% of the first bonds to break in each chain are C-C bonds. Apart from this, the distribution of breaking bonds is fairly uniform over the length of the chain, with the exception of the end bonds, which we have kept as harmonic, as is described in Sec. 2. If this is not done, they are about 3 times more likely to break than other bonds.

We can also investigate the relation between the location of the first chain that breaks and the structure of the cross-section of the bundle. We characterise this aspect with the conditional probability of a chain being the first to break given the number of neighbours in the two-dimensional lattice of the cross-section. This is shown in Fig. 20. The outer chains, with few neighbours, are slightly more likely to be the first to break than chains inside the bundle that are surrounded by other chains. As a result, small bundles with relatively many outer chains show signs of yielding earlier than large bundles. Two possible origins of this effect have been considered, i.e., the rugosity of the chain-chain interaction along the longitudinal direction, and the dependence of fluctuations of individual chains on the number of neighbours.

The effect of the bundle size on the Young's modulus or the yield appears to be relatively small. This is likely due to the fact that covalent bonds are much stronger than the other interactions in the system, such as Coulomb and dispersion forces. In polymers, also steric interactions are important, which could affect the

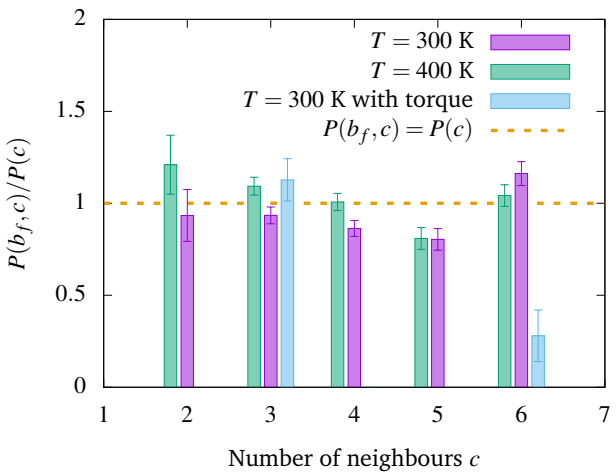

Fig. 20 The ratio of the probability for a chain to break first b_f given that is has c number of neighbouring chains to the probability for a chain to have c neighbouring chains. Two data sets with 100 samples per system with bundles of sizes from $N = 7$ to $N = 24$ at $T = 300$ K and $T = 400$ K respectively are compared to a data set of 100 samples with 7 chains with an external torque at $T = 300$ K. The breaking simulations were carried out with a constant strain rate of 0.8 m/s. The outer chains, with few neighbours, are slightly more likely to be the first to break than chains inside the bundle that are surrounded by other chains. The error bars show the statistical error $\sim 1/\sqrt{n}$.

breaking process through the roughness of the longitudinal chain-chain interaction. We suspect that chain-chain effects would be larger in systems with the stronger inter-molecular interaction compared to bonding between monomers inside the chains.

3.3.3 Winding and defects

In metals, the increase of the yield strength in small systems is related to the absence of localised and especially extended (dislocation) defects. We therefore also briefly investigate here the effect of defects and disorder on the yielding and creep of the fibre bundles.

Figure 10 shows results for several bundles with the same number of chains but different order. One can see that the more unordered cross sections are further away from equilibrium. At the same elongation, some of the chains will not be straight, but twisted around in some way, and subjected to higher forces. Thus one would expect these bundles to break at a shorter elongation, however the force-elongation curves in Figure 11 indicate the opposite.

To investigate this further, bundles of 7 chains was deliberately twisted by applying a torque in the longitudinal direction applied to the two constrained planes. The result of these simulations is shown in Fig. 21. With the added torque, the 6 outer chains are twisted around the central chain. The cross section and side view are shown as well. All the outer chains are rotated about two times around the center. The bundle with torque has a slightly different response during the stretching and breaks significantly earlier than the untwisted bundle, as one would expect. The breaking statistics are included in Fig. 20, and indeed show that the outer chains are by far the most likely to break. The inner chain

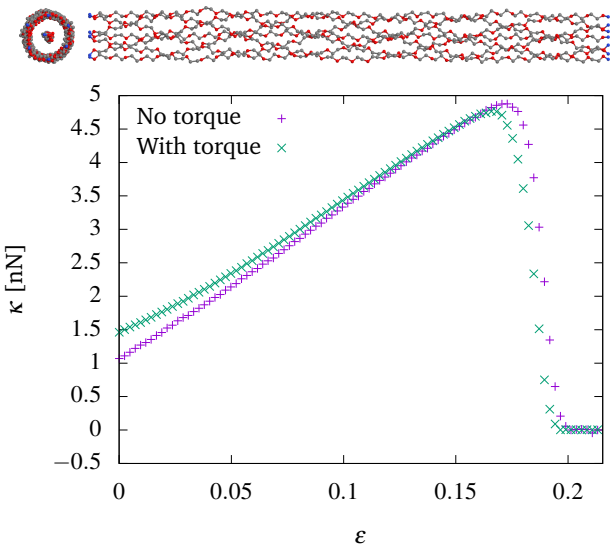

Fig. 21 Comparison of force-elongation curves for bundles with and without added external torque. The samples are stretched at a strain rate of 0.8 m/s at $T = 300$ K. Both curves are averaged over 100 samples of bundles with $N = 7$ chains. Side and front view snapshots are also included at the top.

breaks first in only about 4% of cases.

3.3.4 Parameter dependencies

To asses the value and transferability of the reported findings, it is useful to explore the robustness of the chosen parameters. The role of the strain rate was briefly explored by stretching 100 samples of bundles with 7 chains at $T = 300$ K at a strain rate of 0.4 m/s rather than 0.8 m/s. The average strain at which the first chain breaks then decreased by $0.30 \pm 0.05\%$ compared to the values presented in Fig. 15, which could be reasonably explained by thermal activation of breaking. The estimated rate of chain breaking was similar for the two strain rates, and the estimated Young's modulus was the same within the accuracy reported here.

The choice of bond disassociation energy was briefly challenged by running the same systems with 7 chains with a 8% reduced bond disassociation energy, again with a strain rate of 0.4 m/s at $T = 300$ K. Lowering the disassociation energy increases the role of thermal activation of breaking, and these computations suggests that the rate of chain breaking then is closer to what was reported for $T = 400$ K in Fig. 19. The average strain at which the first chain in the bundles broke decreased by about 1%, while the Young's modulus again was the same within the accuracy reported here. An in-depth study on the role of the bond disassociation energy on the breaking of nanofibres could be an interesting future project.

4 Summary and conclusions

We have investigated stretching and breaking of nano-scale polymer bundles using computer simulations based on an empirical atomistic force field and on a density functional approximation. Simulated nanometrically thin bundles of PEO chains were subjected to tensile load up to their failing.

The density functional (DF) simulations have been performed for small systems, aiming at providing data to benchmark the empirical force field, and to explore features such as re-bonding after breaking that are not accounted for by the force field model. Over a broad range of strain, the DF computations reveal a complex picture. Stretching is resisted at first by torsional restoring forces, and later by bending and stretching.

Stretching of a single chain consisting of ten PEO monomers at $T = 0$ K provides an ab-initio estimate of the energy versus strain relation. The results show that in the low-load limit the energy curve is not simply parabolic, because of the interplay of dihedral, bending and stretching terms determined by rather different force constants. At intermediate strain, where bending and stretching dominate the system response, the simulation provides a high estimate of the Young's modulus that approaches the values measured for oriented carbon protuberances and graphene.

Under conditions of constant strain, a single chain has a broad range of metastability even beyond the length of maximum restoring force, due to the absence of lateral interactions that might perturb the linear arrangement of the chain. The picture is already changed by increasing the system size to two parallel chains, which surprisingly break at a shorter length and load than the single chain. The chains are not perfectly in registry along their common longitudinal direction due to the intra-chain interaction and the helical structure of the chains, giving rise to multiple local minima in the potential energy. The proximity of the two PEO chains opens the way to chemical rebonding after breaking, resulting in a sample made of free floatingăepoxide monomers, and PEO segments terminated by -OH on oneăside, and by planar -OCH2 on the other side. This partial healing might be affected by the approximate DF approach in tackling open shell species, and by the idealised setting of simulations, neglecting defects and impurities.

At the DF level, the limit of thick bundles has been investigated by stretching a system made of the experimental unit cell periodically repeated in space. In this case the stress-strain relation is more linear down to low load, and the bundle breaks at an even shorter length and load than the two-chains system. There are obviously many effects in the chemistry of the chains that are not captured by the classical force field. However, by comparing the behavior of the bond stretching and bending at high strain, we conclude that the classical force field captures sufficiently well the behavior of the single chain under high strain up to the breaking point.

To investigate larger bundles of up to 24 chains of 33 PEO monomers, and one case of 100 chains, we have used molecular-dynamics simulations. The classical force field in our simulations uses a standard functional form for the system potential energy, slightly modified in its stretching term to allow for breaking of C-C and C-O covalent bonds. The bundles are stretched out using two opposed planar structureless clamps. This geometry is greatly simplified with respect to the structure of macroscopic polymers but it is considered to provide a sufficiently realistic picture of bundles of nanometric and sub-nanometric diameter under tension. Moreover, it allows us to isolate and study the effect of the interaction between chains.

We have first determined the bundle geometry and structure

under moderate tension at zero temperature, at ambient temperature and slightly beyond, reaching up to 400 K. Beyond a moderate load of the order of 1 nN per chain, the PEO chains tend to align in the lateral direction, although they retain in part their spontaneous helicity. When the chains are aligned like this, the cross section of the fibre shows a clear structure of a 2D cluster, that at low temperature is arranged according to a hexagonal pattern.

Bundle properties depend on the number N of chains in a non-monotonic way, and are marked by steps at discrete sizes that correspond to the filling of shells in the 2D hexagonal cluster, representing the analog of magic sizes in the physics of nanoclusters.[46,47] We obtain the strain versus load relation of the bundles, from which the Young's modulus, the elastic range and the limiting strength have been determined. Deviations from linear elasticity first occur upwards, corresponding to the stiffening of the bundle due to an-harmonic interactions. At 95% of the limiting load the stress-strain relation bends downwards, and the stress vanishes over a narrow strain range where the bundles break.

Finally, we have simulated the failing of the bundles under load slowly increasing towards the limiting resistance value. This last computational experiment targets creep, but given the large ratio of cohesive to thermal energies, together with the limited time covered by MD, simulations closely approach the mechanical breaking process.

The PEO bundles display a remarkably high tensile strength. The ultimate stress was computed from the MD simulations to be 36.9 ± 0.3 GPa at low temperature, 30.5 ± 0.1 GPa at 300 K and 28.4 ± 0.1 GPa at 400 K, displaying a moderate temperature dependence. The estimated Young's modulus is also high, with DF computations up to 80 GPa at low strain, and about 250 GPa at intermediate strain. The fibres in the MD computations exhibited a modulus of $Y = 144 \pm 6$ GPa at low temperature, around 130 GPa at $T = 300$ K and 125 GPa at $T = 400$ K. As discussed in Sec. 3.2.2, the high strength and stiffness are due to the the semi-crystalline state of the fibres, resulting in samples displaying mechanical properties closer to that of crystalline PE, or even steel. The matching of helical chains that locally is an essential structural feature of extended PEO systems at vanishing or low strain is heavily dominated by the stretching, and the tensile properties are limited primarily by the covalent bonds.

Our study of the relation between the location of the first chain that breaks and the structure of the cross-section of the bundle revealed that outer chains are significantly more likely to be the first to break than chains inside the bundle that are surrounded by other chains. Applying a torque on a set of samples emphasized this effect.

We have investigated the effect of defects in the structure and deviations from the ideal perfect bundles. Defects affect the ultimate strength of the bundles and are present down to the lowest temperatures. We have identified a number of different types of defects, such as chains twisting around the elongation axis, non-optimal 2D isomers and 2D twinning of nanocrystals. At and above ambient temperature all these types of defects form and disappear in a dynamical fashion, rounding the steps at the shell closing sizes, but up to at least 400 K the system retains a high degree of ordering and a recognisable hexagonal structure. Ordering and tight packing of chains increase with increasing load.

The impact of the defects on the ultimate strength of the bundles is nontrivial. In general, non-optimal isomers appear to increase the strength somewhat. This observation is reminiscent of mechanical hardening in metals. However, the two effects are not obviously related, since hardening in metals is caused by defects blocking the movement of dislocations, while in our system dislocation dynamics does not play an obvious role in the yield.

Finally, the thermal activation of chain breaking was investigated, and a Kramer's-type expression for the breaking rate was proposed and compared to simulation data. This expression was based on a highly simplified picture, but nevertheless provides a reasonable description of the data. Moreover, it gives us a mean to extrapolate breaking rates and creep to different conditions.

PEO is a relatively simple polymer, and the results obtained in this work demonstrate quite general properties. Thus, we expect similar behaviour to appear in many other more complex materials that form bundles. However, the chain-chain interactions are relative weak in PEO when compared to the bonds inside the chain. The effects of the structure and chain-chain interaction may thus be substantially bigger in bundles consisting of more strongly interacting chains.

Acknowledgments

This work has been supported by the National Infrastructure for Computational Science in Norway (UNINETT Sigma2) with allocation NN9573K. EB acknowledge The Research Council of Norway for NFR project number 250158 and 262644. The authors are grateful to Prof. Pietro Ballone for his support and many interesting and illuminating discussions.

References

1 J. R. Fried, *Polymer science and technology*, Prentice Hall, 2014.

2 J. M. J. M. Berg, J. L. Tymoczko, L. Stryer and L. Stryer, *Biochemistry*, W.H. Freeman, 2002.

3 G. Strobl, *The physics of polymers: Concepts for understanding their structures and behavior*, 2007.

4 C. Bustamante, Z. Bryant and S. B. Smith, *Ten years of tension: single-molecule DNA mechanics*, 2003.

5 F. Oesterhelt, M. Rief and H. E. Gaub, *New Journal of Physics*, 1999, **1**, year.

6 T. Hugel, M. Rief, M. Seitz, H. E. Gaub and R. R. Netz, *Physical Review Letters*, 2005, **94**, 048301.

7 Kenry and C. T. Lim, *Progress in Polymer Science*, 2017, **70**, 1–17.

8 D. S. Boudreaux, *Journal of Polymer Science Part A-2: Polymer Physics*, 1973, **11**, 1285–1292.

9 H. Matsuura and T. Miyazawa, *Polymer Letters*, 1969, **7**, 65–66.

10 T. Kurita, Y. Fukuda, M. Takahashi and Y. Sasanuma, *ACS Omega*, 2018, **3**, 4824–4835.

11 J. M. Harris, *Poly(Ethylene Glycol) Chemistry: Biotechnical and Biomedical Applications*, Ed. Plenum Press, New York, 1992.

12 L. M. Bellan, J. Kameoka and H. G. Craighead, *Nanotechnology*, 2005, **16**, 1095–1099.

13 G. Linga, P. Ballone and A. Hansen, *Physical Review E*, 2015, **92**, 022405.

14 X. Wu, R. J. Moon and A. Martini, *Cellulose*, 2014, **21**, 2233–2245.

15 S. Plimpton, *Journal of Computational Physics*, 1995, **117**, 1–19.

16 C. Chen, P. Depa, V. G. Sakai, J. K. Maranas, J. W. Lynn, I. Peral and J. R. D. Copley, *Journal of Chemical Physics*, 2006, **124**, 234901(11).

17 W. L. Jorgensen, D. S. Maxwell and J. Tirado-Rives, *Journal of the American Chemical Society*, 1996.

18 B. R. Brooks, R. E. Bruccoleri, B. D. Olafson, D. J. States, S. Swaminathan and M. Karplus, *Journal of Computational Chemistry*, 1983, **4**, 1–31.

19 H. A. Lorentz, *Annalen der Physik*, 1881, **248**, 127–136.

20 M. K. Beyer, *Journal of Chemical Physics*, 2000, **112**, 7307–7312.

21 A. C. Van Duin, S. Dasgupta, F. Lorant and W. A. Goddard, *Journal of Physical Chemistry A*, 2001.

22 A. van Zon, B. Mos, P. Verkerk and S. de Leeuw, *Electrochimica Acta*, 2001, **46**, 1717–1721.

23 S. Neyertz, D. Brown and J. O. Thomas, *Journal of Chemical Physics*, 1994, **101**, 10064.

24 P. J. Steinbach and B. R. Brooks, *Protein simulation below the glass-transition temperature. Dependence on cooling protocol*, 1994.

25 A. Hansen, P. C. Hemmer and S. Pradhan, *The Fiber Bundle Model: Modeling Failure in Materials*, Wiley-VCH, Weinheim, 2015, pp. 1–236.

26 D. Marx and J. Hutter, *Modern Methods and Algorithms of Quantum Chemistry*, John von Neumann Institute for Computing, Jülich, 2000, vol. 3, pp. 329–477.

27 CPMD, *Copyright IBM Corp 1990-2019, Copyright MPI für Festkörperforschung Stuttgart 1997-2001*, `http://www.cpmd.org/`.

28 J. P. Perdew, K. Burke and M. Ernzerhof, *Physical Review Letters*, 1996, **77**, 3865–3868.

29 N. Troullier and J. L. Martins, *Physical Review B*, 1991, **43**, 1993–2006.

30 S. Grimme, J. Antony, S. Ehrlich and H. Krieg, *Journal of Chemical Physics*, 2010, **132**, 130901.

31 Y. Takahashi and H. Tadokoro, *Macromolecules*, 1973, **581**, 5–8.

32 C. M. Breneman and K. B. Wiberg, *Journal of Computational Chemistry*, 1990, **11**, 361–373.

33 T. A. C. G. Capaccio and I. M. Ward, *Journal of Polymer Science*, 1976, **14**, 1641–1658.

34 J. C. L. Hageman, R. J. Meier, M. Heinemann, and R. A. de Groot, *Macromolecules*, 1997, **30**, 5953–5957.

35 M. A. Al-Nasassrah, F. Podczeck and J. M. Newton, *European Journal of Pharmaceutics and Biopharmaceutics*, 1998, **46**, 31–38.

36 G. Stan, F. W. Delrio, R. I. MacCuspie and R. F. Cook, *Journal of Physical Chemistry B*, 2012, **116**, 3138–3147.

37 A. Y. Jee, H. Lee, Y. Lee and M. Lee, *Chemical Physics*, 2013, **422**, 246–250.

38 H. Staudinger, *Die Hochmolekularen Organischen Verbindungen - Kautschuk und Cellulose -*, Springer Berlin Heidelberg, Berlin, Heidelberg, 1932, pp. 105–123.

39 I. Sakurada and K. Kaji, *Journal of Polymer Science Part C*, 1970, **31**, 57–76.

40 H. Matsuura and T. Miyazawa, *Bulletin of the Chemical Society of Japan*, 1968, **41**, 1798–1808.

41 Cambridge University Engineering Departement, *Materials Data Book*, 2003.

42 P. J. Barham and A. Keller, *Journal of Materials Science*, 1985, **20**, 2281–2302.

43 B. Du, J. Liu, Q. Zhang and T. He, *Polymer*, 2001, **42**, 5901–5907.

44 S. Suhai, *Journal of Chemical Physics*, 1986, **84**, 5071–5076.

45 J. Yao, C. Bastiaansen and T. Peijs, *Fibers*, 2014, **2**, 158–186.

46 W. D. Knight, K. Clemenger, W. A. De Heer, W. A. Saunders, M. Y. Chou and M. L. Cohen, *Physical Review Letters*, 1984, **52**, 2141–2143.

47 M. Brack, *Reviews of Modern Physics*, 1993, **65**, 677–732.